Revision 2 correction date 17.12.2018

Cation ordering, valence states and symmetry breaking in the crystal-chemically complex mineral chevkinite-(Ce), Part I: X-ray diffraction and photoelectron spectroscopy studies, and mechanisms of Nb enrichment

MARCIN STACHOWICZ[1,2,*], BOGUSŁAW BAGIŃSKI[1], MARK D. WELCH[2], PAVEL M. KARTASHOV[3], RAY MACDONALD[1], JACEK BALCERZAK[4], JACEK TYCZKOWSKI[4], AND KRZYSZTOF WOŹNIAK[5]

[1]Institute of Geochemistry, Mineralogy and Petrology, University of Warsaw, 02-089 Warsaw, Poland.

[2]Department of Earth Sciences, The Natural History Museum, London SW7 5BD, United Kingdom

[3] Institute of Ore Deposits, Russian Academy of Sciences, Moscow 109107, Russia

[4]Department of Molecular Engineering, Faculty of Process and Environmental Engineering, Lodz University of Technology, 90-924 Łódź, Poland

[5]Biological and Chemical Research Centre, Chemistry Department, University of Warsaw, 02-089 Warsaw, Poland.

ABSTRACT

The crystal structures of natural Nb-rich chevkinite-(Ce) from the Biraya rare-metal deposit, Russia, crystallising in space groups *C*2/*m* and *P*2$_1$/*a*,, were solved and refined to R_1 = 0.03 and R_1 = 0.07, respectively, from data collected with a single-crystal diffractometer. X-ray photoelectron spectroscopy was used to determine the oxidation states of the following ions: Ce^{3+} , Fe^{2+} and Fe^{3+} ; Ti^{4+} and Ti^{3+}. Typically, Nb-rich chevkinite-(Ce) has space group *C*2/*m*, but specimens with space group *P*2$_1$/*a* were also identified. While XPS shows that both

*C*2/*m* and *P*2$_1$/*a* crystal structures contain Ti^{4+} and Ti^{3+}, it also indicates that Ti^{2+} may occur in the *P*2$_1$/*a* phases. The general formula for the Nb-rich chevkinite-(Ce) having space group *C*2/*m* is:

$(Ce^{3+},La^{3+},Nd^{3+},Pr^{3+},Ca^{2+},Na^{+})_{\Sigma4}Fe^{2+}(Fe^{3+},Nb^{5+},Al^{3+})_{\Sigma2}(Ti^{4+},Ti^{3+},Nb^{5+},Mg^{2+})_{\Sigma2}(Si_2O_7)_2O_8$, and

with *P*2$_1$/*a*,

$(Ce^{3+},La^{3+},Nd^{3+},Pr^{3+},Ca^{2+},Na^{+})_{\Sigma4}(Fe^{2+},Mg^{2+},Ti^{2+})_{\Sigma1}(Fe^{3+},Nb^{5+},Al^{3+})_{\Sigma2}(Ti^{4+},Ti^{3+},Nb^{5+})_{\Sigma2}(Si_2O_7)_2O_8$.

It is proposed that, in addition to the substitution $^{C}Fe^{3+} + {}^{D}Ti^{4+} \leftrightarrow {}^{C}Fe^{2+} + {}^{D}Nb^{5+}$, niobium can also be incorporated into chevkinite-(Ce) by the substitution $2^{D}Ti^{4+} \leftrightarrow {}^{D}Nb^{5+} + {}^{D}Ti^{3+}$, leading to substantial Nb-enrichment. The study has revealed that the distribution of cations between the various structural sites is considerably more complex than that envisaged in standard models of the chevkinite group, and that cations such as Ti can have more than one valency in the structure. Lighter elements with larger ionic radii (Mg^{2+}) tend to occupy the *D* site in the *C*2/*m* crystal structure, whereas in the *P*2$_1$/*a* structure these elements (Mg^{2+}, Ti^{2+}) tend to enter the *B* site. Niobium is distributed between the *C* and *D* sites. The techniques employed provide a comprehensive representation of the distribution of cations and can be used to examine similar complexity in other mineral groups. The present study has shown that Nb can be fractionated also from residual melts.

Keywords: Chevkinite-(Ce), niobium, crystal structure, EPMA, X-ray photoelectron spectroscopy, chevkinite-group minerals, the Biraya depostit, Russia

INTRODUCTION

Chevkinite-group minerals (CGM), comprising twelve species, are accessory phases in a wide range of igneous and metamorphic rocks (Macdonald and Belkin 2002; Vlach and Gualda 2007; Carlier and Lorand 2008; Belkin et al. 2009; Macdonald et al. 2009, 2012). They are challenging to characterize structurally and compositionally, as they display extensive compositional zonation and considerable metamictisation (due to Th^{4+}), the latter phenomenon usually involving hydration. In only a few CGM with relatively simple compositions and largely unzoned crystals has it been possible to assign cations to particular sites with some certainty (Popov et al. 2001; Sokolova et al. 2004; Holtstam et al. 2017).

Zoning and metamictisation can lead to considerable difficulties in reconciling compositions derived by electron microprobe analysis (EPMA) with those obtained by refinement of site occupancies from single-crystal XRD. This significant problem was discussed in detail by Sokolova et al. (2004) in their study of radiation-damaged chevkinite-(Ce). These authors also showed that thermal annealing of partially metamict chevkinite-(Ce) in air at 1100 ºC for 3 h resulted in a considerable improvement in the refined site-scattering values (*ssv* = electrons per site) that allowed a more meaningful assignment of site occupancies.

In this paper we report the structural characterization of natural Nb-rich chevkinite-(Ce) having space groups $C2/m$ and $P2_1/a$ from the same hand specimen, with a view to understanding the origin of the $C \rightarrow P$ structural transition. Both crystals studied are compositionally zoned and partially metamict. Given the reported difficulty in correlating electron microprobe analyses with site-scattering values for such crystals (Sokolova et al. 2004), which was also observed in our study, our main aim was to identify the possible coupled substitution mechanisms responsible for the substantial Nb enrichment of these samples of chevkinite-(Ce). We have identified a new substitution mechanism for Nb incorporation that involves Ti^{3+}. This new mechanism can lead to substantial Nb enrichment in chevkinite-(Ce).

The general formula of the CGM is (Popov et al. 2001; Sokolova et al. 2004; Chukanov et al. 2012; Holtstam et al. 2017): $A_4M_5(Si_2O_7)_2O_8$, where A = Ce, La, Sr; M = Fe^{2+}, Fe^{3+}, Ti, Mn, Mg, Zr, Cr, W, □ (where □ denotes cation vacancy). The general formula of CGM was also referred to as $A_4BC_2D_2(Si_2O_7)_2O_8$ (Ito 1967). Based on structural features the chevkinite group can be divided into two subgroups: chevkinite and perrierite.

The chevkinite structure is shown in Figure 1. Site connectivities are shown in Figure 2, which relates the site notation to the chemical formula. Our unique site names *B*, *C*, *D*(1) and *D*(2) correspond to *M*(1), *M*(2), *M*(3) and *M*(4), respectively, of Sokolova et al. (2004). Chains of CO_6 edge-sharing octahedra share corners with the chains of DO_6 edge-sharing octahedra, forming a sheet of octahedra oriented parallel to (001). BO_6 octahedra link with (Si_2O_7) groups to form a heteropolyhedral sheet parallel to (001). The two types of sheet alternate along the Z-direction. Intersheet connectivity is provided *via* tetrahedra and CO_6 octahedra in a way that creates large cavities between the sheets, which are occupied by *A*-cations arranged in a planar hexagonal array.

Niobium is commonly present in low concentrations in CGM ($Nb_2O_5 \leq 5$ wt%) and is assigned to the *C* (*M*(2)) site (Popov et al. 2001; Sokolova et al. 2004) and to *C* and *D (M*(2)-*M*(4)) (Yang et al. 2002, 2007). Makarochkin et al. (1959) described as *niobochevkinite* a mineral from the Ilmen Mineralogical Reserve, southern Urals, where it occurs in a fenitised granitic pegmatite; the phase contains 7.4 wt.% Nb_2O_5, corresponding to 0.71 Nb atoms per formula unit (*apfu*). Popov et al. (2001) described a new mineral from the Ilmen Mountains, southern Urals, Russia, which they termed polyakovite-(Ce) ($(REE,Ca)_4(Mg,Fe^{2+})(Cr^{3+},Fe^{3+})_2(Ti,Nb)_2Si_4O_{22}$). The mineral contains 3.98 wt.% Nb_2O_5 and Nb was allocated as Nb^{5+} to the *C (M2)* site, where the atomic Ti^{4+}/Nb^{5+} ratio is 4.75:1. Here we present the results of electron microprobe analyses and a structural determination of a CGM from Biraya, Russia, which has an average Nb_2O_5 content of 10.19 wt.% and a Ti/Nb atomic ratio is 1.1:1. This is the most Nb-rich CGM yet recorded. The Biraya material is used to examine the following aspects of the CGM; (i) how the entry of Nb affects the structure of the host mineral, (ii) to identify space groups, (iii) how the unique sites in the crystal structure correspond to the chemical formula of Nb-rich chevkinite-(Ce), (iv) and whether or not any cations are present in more than one valence state. Several techniques are employed, including single crystal X-ray diffraction (XRD), EPMA and X-ray photoelectron spectroscopy (XPS).

Coupled substitutions in chevkinite

In order to facilitate the description of compositional data and site occupancies in the Nb-rich chevkinite-(Ce) described here, we outline the coupled substitutions that are likely to be relevant. Initially, we do not consider the possibility of structural vacancies at metal sites (Holtstam et al. 2017), but focus on end-members that are likely to control Nb incorporation into chevkinite. An important constraint is that for electroneutrality the total charge at the metal sites *B*, *C* and *D* is 16+. We present evidence for a new substitution involving trivalent Ti: $2\,^{D}Ti^{4+} \rightarrow {}^{D}Ti^{3+} + {}^{D}Nb^{5+}$, implying a new end-member $^{A}Ce_4\,^{B}Fe^{2+}\,^{C}Fe^{3+}_2\,^{D}(Nb^{5+}\,Ti^{3+})\,Si_4O_{22}$.

A composition approaching that of the Nb-rich chevkinite-(Ce) studied here can be derived from an end-member $^{A}Ce_4\,^{B}Fe^{2+}\,^{C}Fe^{3+}_2\,^{D}Ti^{4+}_2\,Si_4O_{22}$ by:

$+\,0.5\,[2\,^{D}Ti^{4+} \rightarrow {}^{D}Ti^{3+} + {}^{D}Nb^{5+}] + 0.5\,[^{C}Fe^{3+} + {}^{D}Ti^{4+} \rightarrow {}^{C}Fe^{2+} + {}^{D}Nb^{5+}]$

$= {}^{A}Ce_4\,^{B}Fe^{2+}\,^{C}(Fe^{3+}_{1.5}\,Fe^{2+}_{0.5})\,^{D}(Nb^{5+}\,Ti^{3+}_{0.5}\,Ti^{4+}_{0.5})\,Si_4O_{22}$.

While divalent cations are not usually assigned to the *C* site of chevkinite-(Ce), there appear to be no crystal-chemical reasons precluding this possibility. The oxygen bond-valence deficit arising from replacement of an M^{3+} by M^{2+} (around 0.17 *vu*) could, in principle, be accommodated by shortening of the two *A*-O bonds, as well as the additional bond-valence contributed by Nb^{5+} replacing Ti^{4+}.

Metal site vacancies

Vacancies at metal sites in the crystal structure of chevkinite have been reported for the *A*, *B* *C* and *D* sites (Yang et al. 2002), and at *C* (*M*(*2*)) site only, varying from being minor (Popov et al. 2001; Sokolova et al. 2004) to 50% vacancies at this site per formula unit in the crystal structure of delhuyarite-(Ce) that is species-defining (Holtstam et al. 2017).

Consideration of the structure topology of chevkinite (Figs. 1 and 2) indicates that the most plausible metal sites for vacancies are those not bonded to SiO_4 tetrahedra, namely *D*(1) and *D*(2). The *B* site is coordinated to six SiO_4 tetrahedra, and the *C* site is coordinated to two SiO_4 tetrahedra. Formation of a vacancy at the *B* site (replacing a divalent or trivalent cation) or *C* sites results in significant under-bonding by ~ 0.3–0.5 valence units (*vu*) of oxygen atoms shared with tetrahedra. This bond-valence deficit cannot be compensated by protonation of these oxygens as it would result in significant *over*-bonding.

The replacement of Ti^{4+} by a vacancy at the *C* site results in a bond-valence deficit of ~0.7 *vu* for each oxygen atom of the octahedron. This deficit could be compensated by protonation of the four oxygen atoms, i.e. $Ti^{4+} + 4O^{2-} \rightarrow \text{vacancy} + 4OH^{-}$. However, the remaining two oxygen atoms, each bonded to a SiO_4 tetrahedron and two *A* cations, remain significantly under-bonded. Such under-bonding is not, however, enough to allow protonation of these oxygens. Furthermore, protonation of all six oxygens of the vacant CO_6 octahedron lacks a charge-balanced substitution. Thus, it seems unlikely that the *C* site will host vacancies.

The *D*(1,2) sites are not bonded to tetrahedra, but are connected *via* corners to four CO_6 octahedra, and to two DO_6 octahedra with which they share two edges (Fig. 2a). Each oxygen atom of a DO_6 octahedron is shared by two *D* sites, one *A*(1) site and one *A*(2) site (Fig. 1).

Hence, the formation of a *D*-site vacancy would result in a decrease of bond valence of around 0.5-0.7 *vu* (if occupied by M^{3+} or Ti^{4+}) as the affected oxygen would then be three-coordinated *via* one *D*-O and two *A*-O bonds. A protonation mechanism is conceivable if a vacancy replaces Ti^{4+}, as the four oxygen atoms previously shared by two *D* sites would become OH groups *via* $Ti^{4+} + 4O^{2-} \rightarrow \text{vacancy} + 4OH^{-}$. Minor over-bonding associated with protonation could be alleviated by lengthening of *A*-O bonds. Thus, there may be plausible options for vacancy formation at *D* sites.

SAMPLE AND ANALYTICAL METHODS

The Biraya rare-metal deposit is located in the north of the Irkutsk district, Transbaikalia, Russia (57°52′51″N, 116°42′30″E) and comprises a series of lenticular carbonatite bodies and associated fenites, 10 km long and 50-300 m wide. The deposit is thought to be of mid-Palaeozoic age (Chernikov et al. 1994). Preliminary analyses by one of us (PMK) of a CGM from Biraya revealed unusually high Nb_2O_5 contents (up to ~12 wt.%), raising the possibility that this may be a new, Nb-rich member of the group. The sample analysed here (K12) comes from a thin vein in fenites associated with a carbonatite dyke. The vein is zoned and has melanocratic margins rich in tremolite and ferriallanite-(Ce), and a central zone enriched in cordylite. The mineral assemblage includes cordylite-(Ce), cordylite-(La) (Mills et al. 2012), ancylite-(Ce), bastnäsite-(Ce), hydroxylbasnäsite-(Ce), strontianite, daqingshanite-(Ce), Sr-calcite, ferriallanite-(Ce), biraite-(Ce) (Konev et al. 2005), talc and törnebohmite-(Ce).

Mineral compositions were determined by EPMA using wavelength-dispersive spectrometry at the Inter-Institute Analytical Complex at IGMiP Faculty of Geology, University of Warsaw, using a Cameca SX-100 microprobe equipped with four wavelength analysers. The accelerating voltage was 15 kV and the probe current was 40 nA. Counting times were 20 s on peak and 10 s on each of two background positions. The standards and X-ray lines used were: wollastonite for Ca (Kα), rutile for Ti (Kα), corundum for Al (Kα), albite for Na (Kα), diopside for Si and Mg (both Kα), hematite for Fe (Kα), rhodonite for Mn (Kα), barite for Ba (Lα), $SrTiO_3$ for Sr (Lα), synthetic ThO_2 for Th (Mα), apatite Jap2 for P (Kα), zircon ED2 for Zr (Lα), vorlanite for U (Mβ), Nb metal for Nb (Lα), Ta metal for Ta (Mα), LaB6 for La (Lα), CeP_5O_{14} for Ce (Lα), PrP_5O_{14} for Pr (Lβ), NdP_5O_{14} for Nd (Lβ), SmP_5O_{14} for Sm (Lβ), GdP_5O_{14} for Gd (Lβ), REE glasses for Dy (Lβ) and Yb (Lα), and $Y_3Al_5O_{12}$ for Y (Lα). The 'PAP'φ(ρZ) program (Pouchou and Pichoir 1991) was used for corrections. Representative analyses are given in Table 1 and the full data set is in the Supplementary Table 1.

Textural and compositional features of sample K12

The crystal shown in the BSE image on Figure 3a, 150 x 125 μm in area, was used in the structural investigation. The compositional zonation is complex, and is shown diagrammatically in Figure 3b. Our interpretation of the texture is that an originally oscillatory-zoned material (Zone A in Figure 3b) was patchily rimmed by a darker component B, which penetrated into the core of the crystal (Bp). Component B was itself partly rimmed and replaced by a very patchy, microporous component (C). It is unclear whether or not the homogeneous grey wedge (D) was part of the original oscillatory zoning or a later replacement phase. On compositional grounds (below), it is here taken to be part of zone A. It has, however, a sharp contact with the brightest component in the image of the crystal, E.

The major elements (>5 wt% as oxides) are La, Ce, Fe, Si, Nd, Nb and Ti. There is, however, a wide range of elements present at the level of <1 wt% oxides, including Ca, Sr, Ba, Th, U, Sm, Gd, Y, Mn, Mg, Zr and Al. There is considerable compositional variation associated with textural variations. The average compositions of zones A to E are given in Table 1. Variation in the oscillatory zoned area (A+D) is modest, e.g. 8.04-10.09 wt% Nb_2O_5.

In that zone, the average analytical total is 98.03 wt%; however, a notable feature of the other zones is the low oxide totals, down to 88.41 wt% in zone E. Such low totals are commonly associated with hydrothermal alteration, consistent in this case with the textural evidence that the low-total zones appear to be replacing the oscillatory zones. It is also clear from the averages (Table 1), and from the full data set (Supplementary Table 1), that there is a clear negative correlation between the oxide totals and the ThO_2 content. It is known that even small amounts of Th (~0.5 wt%) can cause metamictization of chevkinite (Sokolova et al. 2004). With average ThO_2 contents up to 2.27 wt%, we infer that the crystal is partially metamict and that the areas of higher Th content experienced greater structural damage, permitting access of larger volumes of hydrothermal fluids.

Other compositional changes, registered by the decreasing oxide totals, include: (i) minor decreases in Ca and Sr, followed by a sharp increase into zone E; (ii) minor linear increases in La and Ce, and decreases in Nb and Ti; and (iii) a sharp reduction in Fe and Si contents in zone E.

The compositional variations related to both types of zoning make the calculation of an average composition of the crystal difficult. Here, it is taken to be the average of 54 point analyses of the study sample. An empirical formula based on that average and calculated for 22 oxygen atoms is

$(Ca_{0.18}Sr_{0.13}Na_{0.16}La_{1.2}Ce_{2.02}Pr_{0.16}Nd_{0.42})(Fe_{1.91}Mg_{0.16}Al_{0.13}Ti_{1.22}Nb_{1.11})(Si_{1.99}O_7)_2O_8$.

Experimental

X-ray diffraction

Data collection was undertaken at 100 K on a Rigaku Oxford Diffraction KUMA KM4CCD κ-axis X-ray diffractometer with graphite-monochromated MoKα radiation. A single crystal (crystal 1, Figure 3) was positioned 50 mm from the CCD detector (Opal). 1901 frames were measured with a 1° framewidth and a frametime of 15 sec. Another crystal (no. 2) was measured at 100K on a Rigaku Oxford Diffraction SuperNova diffractometer equipped with X-ray Mo source and Atlas detector. 810 frames were measured with a 1° interval and a counting time of 6 sec. Both data sets were corrected for Lorentz and polarization effects. A numerical absorption correction was applied in both cases. Data reduction and analysis were carried out with the program CrysalisPro® (Rigaku-Oxford Diffraction). Twinning was found for crystal 2 for which 79% of all reflections were indexed for the first component, 46% for the second component and with 26% of reflections overlapped (8% with full overlap) and 1% of reflections remained unindexed. 18% of reflections were almost fully separated, with an overlap factor below 0.2. The threshold to reject overlapped reflections at the twin finalisation process of CrysalisPro® was set to 80% for the preparation of HKLF 4 file. The HKLF 5 file contains a complete set of *hkl*, merged from deconvoluted reflections of both twin domains.

The structures were solved by direct methods and refined using the SHELXL (Sheldrick 2008) within Olex2 (Dolomanov et al. 2009) and WinGX (Farrugia 2012) programs. For the twinned crystal, the HKLF4 file was used for structure solution, followed by structure refinement using the HKLF5 file. The refinements were based on F^2 for all reflections, except those with negative intensities. Weighted *R* factors (*wR*) and all goodness-of-fit (*S*) values are based on F^2. Conventional *R* factors are based on *F* with *F* set to zero for negative F^2. Neutral atomic scattering factors were taken from Tables 4.2.6.8 and 6.1.1.4 of the International Tables for Crystallography Vol. C (Wilson 1992). The *ssv* refined for 4*i*(1) and 4*i*(2) sites were obtained using only the Ce scattering factor, due to the high Ce contents of these sites; the *ssv* for the 2*d* site was based upon Fe and Ti scattering factors; the *ssv* for 2*a*, 2*b*, and 4*e* sites used Ti and Nb neutral scattering factors. When more than one element occupies the same position in the asymmetric unit, constraints for equal atom coordinates and equal anisotropic displacement parameters for these groups of atoms within each unique site were applied. Twinned crystal 2 was refined against HKLF 5 file, containing reflections from both components. Supplementary Table S2 contains selected crystallographic data and refinement details. In order to obtain better geometry and ADPs, higher-resolution datasets were collected to 61° 2θ and 66° 2θ for crystal 1 and crystal 2, respectively. The highest residual electron density (2.7 for crystal 1 and 9.38 eÅ^{-3} for crystal 2) are located *c.a.* 0.6-0.7 Å from the heavy REE atoms. These values can be reduced to 1.5 and 4.8 e/Å^{3} when the resolution is decreased to 0.6 Å^{-1}, (recommended by the International Union of Crystallography), consistent with the cause of the high residual being associated with termination ripples in the Fourier synthesis, rather than being due to incomplete modelling of a contribution from non-bonded electrons or a split site.

X-ray photoelectron spectroscopy

X-ray photoelectron spectroscopy (XPS) analyses were carried out at the Faculty of Process and Environmental Engineering, Lodz University of Technology, Poland, on a Kratos AXIS Ultra spectrometer equipped with a monochromatic Al Kα X-ray source of excitation energy equal to 1486.6 eV. The spectra were obtained using an analysis area of 300 x 700 μm. The power of the anode was set at 225 W and the hemispherical electron energy analyzer was operated at a pass energy of 20 eV for all high resolution measurements. All spectra were collected using a charge neutralizer and every energy region was swept ten times to increase the signal-to-noise-ratio. Evaluation of the XPS data was conducted by using the CasaXPS software. The adventitious carbon main peak (C(1s), 284.8 eV) was used for the final calibration of each spectrum.

RESULTS

Crystal structure refinement

Crystal 1 has space group *C*2/*m* and crystal 2 has space group $P2_1/a$. In the refinement strategy used, the occupancies of the two *A* sites, one *B* (*M*(1)) site, one *C* (*M*(2)) site and two

D (*M*(3), *M*(4)) sites were refined. In the Wyckoff notation these sites have multiplicities of: *A* 4*i* and 4*i* for *C*2/*m*, 4*e* and 4*e* for $P2_1/a$, *B* 2*d* for *C*2/*m*, 2*b* for $P2_1/a$, *C* 4*e* for *C*2/*m*; 4*e* for $P2_1/a$, *D* 2*a* and 2*b* for *C*2/*m*, 2*a* and 2*c* for $P2_1/a$. The *ssv* for crystal 1 (*C*2/*m*) refined to the following values: 4*i*(1) = 52.5 electrons (≡ 0.90 Ce), 4*i*(2) 50.2 (≡ 0.87 Ce), 2*d* = 25.9 electrons (≡0.96Fe + 0.04Ti), 4*e* = 24.4 electrons (≡ 0.60Ti + 0.40Nb), 2*a* = 20.8 electrons (≡ 0.95Ti), 2*b* = 24.5 electrons (≡ 0.87Ti + 0.13Nb). The site scattering values, for crystal 2 ($P2_1/a$), were refined as follows: 4*e*(1) = 52.2 electrons (≡ 0.90Ce), 4*e*(2) = 51.6 electrons (≡0.89Ce), 2*b* = 24.6 electrons (≡ 0.64Fe + 0.36Ti), 4*e* = 22.7 electrons (≡ 0.41Fe + 0.59Ti), 2*a* = 22.7 electrons (≡ 0.96Ti + 0.04Nb), 2*c* = 26.0 electrons (≡0.78Ti+0.22Nb), with multiplicity taken into account. Supplementary Table S3 presents the final atom coordinates.

Stachowicz et al. (in revision) reports the values of the *M*-O bond lengths, the polyhedral volumes of the MO_x first coordination spheres with cations from the *A*, *B*, *C* and *D* sites and refined *ssv* for crystal 1, 2 and seven other Nb-rich chevkinite-(Ce) crystals.

Valence states (XPS)

As Nb-rich chevkinite-(Ce) is very complex compositionally, we now explore the possibility that one or more cations is present in different oxidation states. XPS was used to identify the oxidation states of certain elements. The experiments were carried out to determine how Nb-rich chevkinite-(Ce) maintains electroneutrality. A determination of the oxidation state of Ce and plausible inferred charges of Ti and Fe have proved possible to obtain.

XPS is a surface method in which monochromatic soft X-rays interact with atoms from the surface of the sample by ejecting their core shell electrons. The measured kinetic energy of the emitted electrons gives information about the binding energies of these electrons to the nucleus (after correction towards the work function characteristic for each XPS instrument). The energy of emitted electrons has a characteristic value for particular elements. Moreover, it is also sensitive to oxidation state. A more detailed explanation of the principles of XPS can be found in Moulder et al. (1992) and Heide (2011). An order-of-magnitude smaller sample can be studied compared with Mössbauer spectroscopy.

A signal of so-called "adventitious carbon", used for the calibration of spectra, is almost always a part of the XPS spectra, even if the carbon did not originate in the sample itself. The C(1s) band (maximum at 284.8 eV) is often used for the calibration of narrow scan positions before quantitative analysis. When carbon is absent from a sample, this signal comes from traces of organic molecules on the sample surface. Data were collected from two different areas of the sample surface. For both, the carbon peak maxima were located at the same energy, 284 eV, which was caused by the charge neutralizer. For that reason, all the spectra were shifted by about +0.8 eV before quantitative analysis.

The Ce(3d) spectra (Figure 4) are of good quality with a high signal-to-noise ratio. They are identical for both analysed areas. The shape of all peaks is characteristic of trivalent Ce and their peak positions are in perfect agreement with literature presenting trivalent Ce oxide spectra (Praline et al. 1980; Paparazzo et al. 1991; Mullins et al. 1998; Bêche et al. 2008). The Ti spectra (Figure 5) are also of reasonable quality and can easily be deconvoluted to obtain quantitative information. The spectra show that Ti in Nb-rich chevkinite-(Ce) is in all three oxidation states: +3, +4 and +2, and that the peaks overlap one another. These results may also be compared to studies by Biesinger et al. (2010), where a compilation of XPS data from the literature, such as the positions of particular peaks and the splitting between spin-orbit doublets, has been presented. That analysis was next complemented by an experimental verification for some reference samples. Such an approach gave a good opportunity for comparison in the case of a quantitative analysis of new materials.

Computation of the overlapping peak areas, from which the ratios of valency are obtained, needs some constraints on the fitting procedure to retain physical meaning for the analysed spectra. The constraint applied was that the ratio of areas for the spin-orbit split doublets (Ti(2p)3/2:Ti(2p)1/2) was to be equal to 2:1 for each oxidation state of Ti. An additional constraint for the Ti^{4+}(2p)1/2-Ti^{4+}(2p)3/2 doublet splitting to be equal to 5.5 eV in the spectrum from the first area was necessary. The last constraint was applied to Ti^{2+}3/2 FWHM being equal to 0.8 of Ti^{3+}3/2 FWHM in the spectrum from the second area of the sample. This value was taken from the first spectrum, where Ti^{3+}3/2 peak is dominant and no constraints on the full width at half maxima were applied during the fitting process. The spectra from each binding energy region show different ratios of Ti valency. It is not known exactly what causes this discrepancy. Sputtering by an argon gun, which causes a reduction of some cations, including Ti and Fe (Choudhury et al. 1989; Hassel and Burggraaf 1991; McCafferty and Wightman 1999; Hashimoto and Tanaka 2002), was not carried out in this experiment. The influence of sputtering on Nb-rich chevkinite-(Ce) was tested after the essential measurements. We have not found in the literature any information on surface effects causing a shift of the collected peaks during multiple acquisition, which in the case of Ti could explain this phenomenon.

The applicability of XPS to the investigation of the valency of cations was tested on a number of CGM samples (perrierite-(Ce) from Roseland, Virginia; chevkinite -(Ce) from the Cherry Mts, Southern Urals vein 35; Ilmen Mts, chevkinite-(Ce) from the Ilmen Mts, Southern Urals; and chevkinite-(Ce) from a pegmatite, Diamer District, Pakistan).The charge balance of chemical formulae for all specimens was well established by the combination of EPMA and X-ray diffraction analyses. Spectra for tetravalent Ti were obtained for all these samples. We associate the presence of the lower valency of titanium in the Nb-rich chevkinite-(Ce) to a high concentration of niobium.

The Fe(2p)3/2 envelope containing a high-spin Fe cation was fitted using peaks corresponding to the Gupta and Sen (GS) multiplets formalism (Gupta and Sen 1974, 1975). The multiplets model the splitting of the core p-vacancy levels in iron (in the Hartree-Fock free-ion approximation). GS multiplets are widely used in the quantitative analysis of Fe valency. A review of the positions and widths of Fe peak components and a comparison with the results obtained from reference samples were performed by Grosvenor et al. (2004). The values of the signal to noise ratio for Fe(2p) 3/2 spectra (Figure 6) collected for Nb-rich chevkinite-(Ce) are rather low. Nevertheless, the shape of the experimental spectra can be reproduced very well by the convolution of peaks proposed by Grosvenor et al. (2004). The XPS instrument, AlKα X-ray source and passing energy (20 eV) were identical to those used in the reference experiments of Grosvenor et al. (2004). For that reason the FWHM values, and the distances between peaks belonging to each valency of Fe, were constrained within the limits of deviation, as in the reference article. Such an approach can give only an approximation to the ratios of the oxidation states of Fe in the sample. Here Fe^{3+}:Fe^{2+} was observed to be 1.85:1.

Assignment of cations to crystallographic sites

An exact allocation of ionic compositions (taken from EPMA) to particular unique sites in the crystal structure is a complex matter for several reasons. The previously given empirical formula for Nb-rich chevkinite-(Ce), $(Ca_{0.18}Sr_{0.13}Na_{0.16}La_{1.2}Ce_{2.02}Pr_{0.16}Nd_{0.42})(Fe_{1.91}Mg_{0.16}Al_{0.13}Ti_{1.22}Nb_{1.11})(Si_{1.99}O_7)_2O_8$, was obtained as the average of all 54 EPMA analyses. However, this formula is not representative of the crystalline areas of the sample. Due to a significant concentration of thorium, metamictization of some areas occurred, followed by hydrothermal alteration. Empirical evidence for this can be found in the low totals in the EPMA analyses which include analyses of metamict areas (area E in Figure 3b and column E of Table 1), not representative of the crystalline areas. Further evidence was found in the much stronger diffraction from crystal 1 after annealing at 750 °C in a vacuum environment (Stachowicz et al., in revision), compared with the untreated crystal. Hence, it appears that recrystallization took place during the annealing process. Moreover, a transformation from $C2/m$ to $P2_1/a$ crystal symmetry was observed. Due to partial metamictization of the crystal the EPMA composition does not correspond exactly to the refined site scattering values of positions occupied by cations in the crystal lattice. Finally, the EPMA analysis was performed on only one section of crystal 1 (*ca.* in the middle of the height), and revealed complex and highly variable zoning. Nonetheless, a discussion and an attempt to assign the major elements (exceeding 0.1 *apfu*) to particular sites are now given.

The averages of the compositions of most crystalline parts of the crystal from area A+D and C in Figure 3, being closest to the primary chevkinite, served as a guideline for the assignment of composition in the Nb-rich chevkinite-(Ce) crystal structure. An approximate formula based on EPMA (column A+D and C of Table 1) can then be written as:

$(Ca_{0.11}Na_{0.12}La_{1.30}Ce_{2.06}Pr_{0.16}Nd_{0.42})(Fe_{2.24}Mg_{0.22}Al_{0.15}Ti_{1.06}Nb_{0.98})(Si_{2.07}O_7)_2O_8$.

In order to determine which atoms occupy particular A, B, C and D sites, we related the values of the ionic radii of Shannon (1976) to the volumes of the first coordination polyhedra of the sites, calculated from the X-ray crystal structures using the algorithm of Robinson et al. (1971). The volumes of octahedra were calculated using *Platon* software (Spek 2009) and volumes of other polyhedra using *Vesta* software (Momma and Izumi 2011). The *ssv* were refined against the X-ray data. The refined A, B, C and D *ssv* sum to significantly different values for $C2/m$ and $P2_1/a$ crystal structures. The MO_6 first coordination sphere octahedra, (especially the BO_6 octahedra) also differ in volumes (Stachowicz et al., in revision).

The *A* sites are occupied by *REE* Ca, and Na, atoms. As is common in CGM, there is an excess of elements in the *A* site. Sokolova et al. (2004) suggested the presence of small amounts (0.05 *apfu*) of Ca in the *B* site of chevkinite-(Ce) from the Khaldzan Buragtag alkali granite, Mongolia. This is also a possibility for the Nb-rich chevkinite-(Ce).

The *B*O$_6$ octahedra are the largest in both discussed structures. An increase from 11.9 Å^3 to 12.6 Å^3 was found for *C*2/*m* and *P*2$_1$/*a* structures. The elements with the largest volumes (except cations from the *A* sites) should be considered to occupy to the *B* site, namely Fe^{2+} (i.r.=0.78 Å), Mg^{2+} (i.r.=0.72 Å) and Ti^{2+} (i.r.=0.86 Å). The lighter Mg^{2+} and Ti^{2+} ions are absent from the *C*2/*m* structure and substitute for part of the Fe^{2+} when the structure changes to *P*2$_1$/*a*. This reallocation of cations rationalises the increase of *B*O$_6$ volume and the drop of *ssv* of the *B* site from 25.9 to 24.6.

The *C* site has the smallest volume of all *M*O$_6$ coordination octahedra (Stachowicz. et al. in revision) in both space groups. It is occupied by Fe^{3+} (i.r.= 0.65 Å), Nb^{5+} (i.r.= 0.64 Å) and Al^{3+} (i.r.= 0.54 Å) ions. This site seems to change the least due to transformation.

The two *D* sites of Nb-rich chevkinite-(Ce) are occupied by Ti^{3+} (i.r.= 0.67 Å), Ti^{4+} (i.r.= 0.60 Å), Nb^{5+} and Mg^{2+} in the crystal 1 with *C*2/*m* space group. In the *P*2$_1$/*a* structure of crystal 2, Mg^{2+} is absent in the *D* sites. These *D*O$_6$ octahedra have the largest volumes among all chevkinites of known crystal structure (Stachowicz et al., in revision). We interpret this as a structural indication of the presence of Ti^{3+} (*C*2/*m* and *P*2$_1$/*a*) and Mg^{2+} (*C*2/*m*) at the *D* sites of the Nb-rich chevkinite-(Ce). The lower valency of Ti balances the charge associated with the high content of Nb^{5+}. The migration of Mg^{2+}, the largest among the *D* site ions, results in a decrease of the *D*O$_6$ volume of *ca.* 0.14 Å. The mechanisms of Ti^{4+} substitution in the *D* sites can be summarised as: $2Ti^{4+} \rightarrow Nb^{5+} + Ti^{3+}$; $2Ti^{4+} + O^{2-} \rightarrow Nb^{5+} + Mg^{2+} + OH^{-} + vac.$

Niobium is distributed among the *C* and *D* sites. Its presence is not seen as a larger value of *ssv* because it is masked by the presence of lighter elements, Al^{3+} in the *C* site and Mg^{2+}

and possibly vacancies in the *D* site. With the migration of magnesium to the *B* site in the $P2_1/a$ crystal structure the presence of Nb is revealed in the increasing value of *ssv* in the *D* sites. Here, the *ssv* of the *D*(2) site (2*c* in the Wyckoff notation) refines to a value of 26, which can suggest another interpretation, namely full occupation by Fe. This *ssv* value increases systematically with the degree of transformation to $P2_1/a$ symmetry. This phenomenon is discussed in the companion paper by Stachowicz et al. (in revision).

IMPLICATIONS

The predominant symmetry of Nb-rich chevkinite-(Ce) is $C2/m$; however, a natural specimen of lower, $P2_1/a$, symmetry was also recognised. Despite their nearly identical crystal structure topologies, the partitioning of elements among the *B*, *C* and *D* sites differs significantly for specimens having the different space groups. Lighter elements with larger ionic radii (Mg^{2+}, Ti^{2+}) tend to occupy the *D* site in the $C2/m$ crystal structure, whereas in the $P2_1/a$ structure these elements prefer the *B* site. Niobium is distributed between the *C* and *D* sites. The high content of niobium in the studied mineral may influence the presence of lower valences of titanium through the substitution $2Ti^{4+} \rightarrow Nb^{5+} + Ti^{3+}$, to maintain electroneutrality. It points to the possibile existence of a new chevkinite end member. For Nb-rich chevkinite-(Ce), Ce is present as Ce^{3+}, Fe as Fe^{3+} and Fe^{2+} (in the ratio 1.85:1), and Ti as Ti^{4+}, Ti^{3+} and possibly Ti^{2+}, however only in the transformed $P2_1/a$ form. Our work shows that a combined approach using structure determination (XRD), photoelectron spectroscopy and electron microprobe analysis can provide a comprehensive representation of the distribution of cations, and their oxidation state, in a structurally and chemically complex mineral. Chevkinite-group minerals can occur as phenocrysts in silicic volcanic rocks and can be early-magmatic phases in granites. They thus have the potential to fractionate the wide range of elements in their structure. For example, chevkinite-(Ce) has been the dominant control over Light REE distribution in peralkaline rhyolites from Gran Canaria (Troll et al. 2003) and metaluminous rhyolites of the Peach Spring Tuff, SW USA (Padilla and Gualda 2016). The present study has shown that Nb can also be fractionated from residual melts.

ACKNOWLEDGMENTS

We are very grateful to Stefano Merlino, Sergey Aksenov, an anonymous reviewer and Associate Editor Alejandro Fernandez-Martinez for their very helpful comments on the manuscript, which much improved its quality. The research for this paper was in part supported by the Polish Ministry of Science and Higher Education within the Mobility Plus Fund award number 1301/MOB/IV/2015/0. Financial support was provided by Polish National Science Centre NCN grant decision DEC-2011/03/B/ST10/05491. We thank the Department of Earth Sciences, Natural History Museum, London, for hosting MS's year-long visit to work with MDW.

REFERENCES CITED

Bêche, E., Charvin, P., Perarnau, D., Abanades, S., and Flamant, G. (2008) Ce 3d XPS investigation of cerium oxides and mixed cerium oxide (CexTiyOz). Surface and Interface Analysis, 40, 264–267.

Belkin, H.E., Macdonald, R., and Grew, E.S. (2009) Chevkinite-group minerals from granulite-facies metamorphic rocks and associated pegmatites of East Antarctica and South India. Mineralogical Magazine, 73, 149–164.

Biesinger, M.C., Lau, L.W.M., Gerson, A.R., and Smart, R.S.C. (2010) Resolving surface chemical states in XPS analysis of first row transition metals, oxides and hydroxides: Sc, Ti, V, Cu and Zn. Applied Surface Science, 257, 887–898.

Carlier, G., and Lorand, J.-P. (2008) Zr-rich accessory minerals (titanite, perrierite, zirconolite, baddeleyite) record strong oxidation associated with magma mixing in the south Peruvian potassic province. Lithos, 104, 54–70.

Chernikov, V.V., Konev, A.A., Vorobiev, E.I., Yablonovskii, B.V., and Dneprovskaya, B.V. (1994) Endogenous carbonate rocks of Biraya: a promising source of rare-earth and rare-metal raw material. Geology and Geophysics, 35, 50–60.

Choudhury, T., Saied, S.O., Sullivan, J.L., and Abbot, A.M. (1989) Reduction of oxides of iron, cobalt, titanium and niobium by low-energy ion bombardment. Journal of Physics D: Applied Physics, 22, 1185.

Chukanov, N.V., Blass, G., Pekov, I.V., Belakovskiy, D.I., Van, K.V., Rastsvetaeva, R.K., and Aksenov, S.M. (2012) Perrierite-(La), (La,Ce,Ca)4(Fe2+,Mn)(Ti,Fe3+,Al)4(Si2O7)2O8, a new mineral species from the Eifel volcanic district, Germany. Geology of Ore Deposits, 54, 647–655.

Dolomanov, O.V., Bourhis, L.J., Gildea, R.J., Howard, J.A.K., and Puschmann, H. (2009) *OLEX2* : a complete structure solution, refinement and analysis program. Journal of Applied Crystallography, 42, 339–341.

Farrugia, L.J. (2012) WinGX and ORTEP for Windows: an update. Journal of Applied Crystallography, 45.

Grosvenor, A.P., Kobe, B.A., Biesinger, M.C., and McIntyre, N.S. (2004) Investigation of multiplet splitting of Fe 2p XPS spectra and bonding in iron compounds. Surface and Interface Analysis, 36, 1564–1574.

Gupta, R., and Sen, S. (1974) Calculation of multiplet structure of core p-vacancy levels. Physical Review B, 10, 71–77.

Gupta, R.P., and Sen, S.K. (1975) Calculation of multiplet structure of core p-vacancy levels. II. Physical Review B, 12, 15–19.

Hashimoto, S., and Tanaka, A. (2002) Alteration of Ti 2p XPS spectrum for titanium oxide by low-energy Ar ion bombardment. Surface and Interface Analysis, 34, 262–265.

Hassel, B.A. van, and Burggraaf, A.J. (1991) Oxidation state of Fe and Ti ions implanted in yttria-stabilized zirconia studied by XPS. Applied Physics A, 52, 410–417.

Heide, P. van der (2011) X-ray Photoelectron Spectroscopy: An introduction to Principles and Practices, 220 p. John Wiley & Sons.

Holtstam, D., Bindi, L., Hålenius, U., and Andersson, U.B. (2017) Delhuyarite-(Ce) – Ce4Mg(Fe3+2W)□(Si2O7)2O6(OH)2 – a new mineral of the chevkinite group, from the Nya Bastnäs Fe–Cu–REE deposit, Sweden. European Journal of Mineralogy, 29, 897–905.

Holtstan, D., Bindi, L., Halenius, U., and Andersson, U.B. (2017, September) Delhuyarite-(Ce) - $Ce_4Mg(Fe^{3+}{}_2W)(Si_2O_7)_2O_6(OH)_2$ - a new mineral of the chevkinite group, from the Nya Bastnäs Fe-Cu-REE deposit, Sweden. Text.

Ito, J. (1967) The study of chevkinite and perrierite. The American Mineralogist, 52, 1094–1104.

Konev, A., Pasero, M., Pushcharovsky, D., Merlino, S., Kashaev, A., Suvorova, L., Ushchapovskaya, Z., Nartova, N., Lebedeva, Y., and Chukanov, N. (2005) Biraite-(Ce), $Ce_2Fe^{2+}CO_3)(Si_2O_7)$, a new mineral from Siberia with a novel structure type. European Journal of Mineralogy, 17, 715–721.

Macdonald, R., and Belkin, H.E. (2002) Compositional variation in minerals of the chevkinite group. Mineralogical Magazine, 66, 1075–1098.

Macdonald, R., Belkin, H.E., Wall, F., and Bagiński, B. (2009) Compositional variation in the chevkinite group: new data from igneous and metamorphic rocks. Mineralogical Magazine, 73, 777–796.

Macdonald, R., Bagiński, B., Kartashov, P., Zozulya, D., and Dzierżanowski, P. (2012) Chevkinite-group minerals from Russia and Mongolia: new compositional data from metasomatites and ore deposits. Mineralogical Magazine, 76, 535–549.

Makarochkin, B.A., Gonibesova, K.A., and Makarochkina, M.S. (1959) Chevkinite from the Ilmen Mountains. Zapiski Vserossiiskogo Mineralogicheskogo Obshchestva USSR, 88, 574–553.

McCafferty, E., and Wightman, J.P. (1999) An X-ray photoelectron spectroscopy sputter profile study of the native air-formed oxide film on titanium. Applied Surface Science, 143, 92–100.

Mills, S.J., Kartashov, P.M., Kampf, A.R., Konev, A.A., Koneva, A.A., and Raudsepp, M. (2012) Cordylite-(La), a new mineral species in fenite from the Biraya Fe–REE deposit, Irkutsk, Russia. The Canadian Mineralogist, 50, 1281–1290.

Momma, K., and Izumi, F. (2011) *VESTA 3* for three-dimensional visualization of crystal, volumetric and morphology data. Journal of Applied Crystallography, 44, 1272–1276.

Moulder, J.F., Stickle, W.F., Sobol, P.E., and Bomben, K.D. (1992) Handbook of X-ray photoelectron spectroscopy Vol. 40. Perkin Elmer Eden Prairie, MN.

Mullins, D.R., Overbury, S.H., and Huntley, D.R. (1998) Electron spectroscopy of single crystal and polycrystalline cerium oxide surfaces. Surface Science, 409, 307–319.

Padilla, A.J., and Gualda, G.A. (2016) Crystal-melt elemental partitioning in silicic magmatic systems: an example from the Peach Spring Tuff high-silica rhyolite, Southwest USA. Chemical Geology, 440, 326–344.

Paparazzo, E., Ingo, G.M., and Zacchetti, N. (1991) X-ray induced reduction effects at CeO2 surfaces: An x-ray photoelectron spectroscopy study. Journal of Vacuum Science & Technology A, 9, 1416–1420.

Popov, V.A., Pautov, L.A., Sokolova, E., Hawthorne, F.C., McCammon, C., and Bazhenova, L.F. (2001) Polyakovite-(Ce),(REE, Ca)$_4$(Mg, Fe^{2+})(Cr^{3+}, Fe^{3+})$_2$(Ti, Nb)$_2$Si$_4$O$_{22}$, a new metamict mineral species from the Ilmen Mountains, southern Urals, Russia: mineral description and crystal chemistry. The Canadian Mineralogist, 39, 1095–1104.

Pouchou, J.-L., and Pichoir, F. (1991) Quantitative Analysis of Homogeneous or Stratified Microvolumes Applying the Model "PAP." In K.F.J. Heinrich and D.E. Newbury, Eds., Electron Probe Quantitation pp. 31–75. Springer US.

Praline, G., Koel, B.E., Hance, R.L., Lee, H.-I., and White, J.M. (1980) X-Ray photoelectron study of the reaction of oxygen with cerium. Journal of Electron Spectroscopy and Related Phenomena, 21, 17–30.

Robinson, K., Gibbs, G.V., and Ribbe, P.H. (1971) Quadratic Elongation: A Quantitative Measure of Distortion in Coordination Polyhedra. Science, 172, 567–570.

Sanjuan-Szklarz, W.F., Hoser, A.A., Gutmann, M., Madsen, A.Ø., and Woźniak, K. (2016) Yes, one can obtain better quality structures from routine X-ray data collection. IUCrJ, 3, 61–70.

Shannon, R.D. (1976) Revised effective ionic radii and systematic studies of interatomic distances in halides and chalcogenides. Acta Crystallographica Section A, 32, 751–767.

Sheldrick, G.M. (2008) A short history of *SHELX*. Acta Crystallographica Section A Foundations of Crystallography, 64, 112–122.

Sokolova, E., Hawthorne, F.C., Ventura, G.D., and Kartashov, P.M. (2004) Chevkinite-(Ce): Crystal Structure and the Effect of Moderate Radiation-Induced Damage on Site-Occupancy Refinement. The Canadian Mineralogist, 42, 1013–1025.

Spek, A.L. (2009) Structure validation in chemical crystallography. Acta Crystallographica Section D Biological Crystallography, 65, 148–155.

Stachowicz, M., Welch, M.D., Bagiński, B., Kartashov, P.M., Macdonald, R. and Woźniak, K. (2018) Cation ordering, valence states and symmetry breaking in the crystal-chemically complex mineral chevkinite-(Ce), Part II. Recrystallization, transformation and metamict states in chevkinite. American Mineralogist, in revision.

Troll, V.R., Sachs, P.M., Schmincke, H.-U., and Sumita, M. (2003) The REE-Ti mineral chevkinite in comenditic magmas from Gran Canaria, Spain: a SYXRF-probe study. Contributions to Mineralogy and Petrology, 145, 730–741.

Vlach, S.R.F., and Gualda, G.A.R. (2007) Allanite and chevkinite in A-type granites and syenites of the Graciosa Province, southern Brazil. Lithos, 97, 98–121.

Wilson, A.J.C. (1992) International Tables for Crystallography: Mathematical, physical, and chemical tables Vol. 3. International Union of Crystallography.

Yang, Z., Fleck, M., Smith, M., Tao, K., Song, R., and Zhang, P. (2002) The crystal structure of natural Fe-rich chevkinite-(Ce). European Journal of Mineralogy, 14, 969–975.

Yang, Z., Li, H., Liu, M., and Franz, P. (2007) Crystal Chemistry of Iron in Non-Metamict Chevkinite-(Ce): Valence State and Site Occupation Proportions. Journal of Rare Earths, 25, 238–242.

FIGURE CAPTIONS

Figure 1. General view of chevkinite-type structure. Sheets of edge-sharing $C\mathrm{O}_6$, $D(1)\mathrm{O}_6$ and $D(2)\mathrm{O}_6$ octahedra parallel to (001) alternate with layers of $\mathrm{Si_2O_7}$ dimers connected *via* $B\mathrm{O}_6$ octahedra. Framework interstices are occupied by sheets of *A*(1) and *A*(2) sites occupied by REE and dominated by Ce in the samples studied here. Ce at *A*(1) is 8-coordinate in the $C2/m$ and $P2_1/a$ structures. Ce at *A*(2) is 8- and 9-coordinated in the $C2/m$ and $P2_1/a$ structures, respectively. Linkages between the sheets and layers involve Si(2) tetrahedra and Ce-O bonds.

Figure 2. The connectivity of *B*, *C* and *D* octahedra in chevkinite-type structure **(a)** projected onto (001) and **(b)** projected onto (010).

Figure 3. (a) BSE image of the crystal of Nb-rich chevkinite-(Ce) analysed by XRD and by EPMA, to show the very complex internal zonation. **(b)** Simplified interpretation of the distribution of the various textural zones. An oscillatory zoned crystal (Zones A and D) was replaced during one or more phases of hydrothermal alteration (zones B, Bp, C and E) The dark circles are analytical spots.

Figure 4. The Ce^{3+} spectrum is composed of two multiplets corresponding to the spin-orbit split Ce(3d)5/2 and (3d)3/2 core holes. The line shapes and their positions are typical of trivalent Ce. Additionally, there is no peak at 916 eV which is a characteristic of tetravalent Ce.

Figure 5. The deconvoluted Ti(2p)3/2, Ti(2p)1/2 spectra from two different areas of the sample. The ratios of Ti with each oxidation state differ in both experiments. The largest contributions are Ti^{3+} (first exp.) and Ti^{4+} (second exp.). The final occupation ratio included in the X-ray crystal structure is: $Ti^{4+}/Ti^{3+}/Ti^{2+} = 5/5/2$.

Figure 6. The deconvolution of the Fe(2p)3/2 spectra showing the 1.84:1 ratio of Fe^{3+} to Fe^{2+}.

TABLES

Table 1. EPMA average compositions of textural zones.

Zone	**A+D**	**B**	**B$_p$**	**C**	**E**
n	**14**	**8**	**18**	**9**	**5**
wt%					
P_2O_5	0.05	0.15	0.16	0.09	0.11
Nb_2O_5	8.86	11.21	11.57	10.10	7.83
Ta_2O_5	0.10	0.10	0.10	0.10	0.06
SiO_2	18.18	17.11	16.66	17.47	9.48
TiO_2	5.78	7.56	7.53	6.58	5.64
ThO_2	0.47	1.35	1.40	0.95	2.27
$Al2O_3$	0.58	0.44	0.47	0.48	0.08

Sc_2O_3	0.14	0.19	0.15	0.14	0.10
La_2O_3	15.86	12.40	12.04	14.30	17.44
Ce_2O_3	24.70	21.38	21.41	23.48	27.09
Pr_2O_3	2.05	1.68	1.67	1.80	2.00
Nd_2O_3	5.17	4.56	4.65	4.93	5.19
Sm_2O_3	0.33	0.31	0.32	0.27	0.33
Gd_2O_3	0.23	0.31	0.20	0.22	0.25
MgO	0.70	0.36	0.31	0.52	0.06
CaO	0.37	0.72	0.69	0.54	2.00
MnO	0.19	0.34	0.29	0.28	0.16
FeO*	12.33	9.11	8.80	10.31	2.97
SrO	0.49	0.73	0.68	0.53	4.12
BaO	0.51	0.75	1.07	1.00	0.94
PbO	0.58	0.55	0.56	0.73	bd
Na_2O	0.36	0.38	0.39	0.45	0.51
Total	98.03	91.67	91.12	95.27	88.41

FeO*, all Fe as Fe^{2+}; bd, below detection; *n*, number of analyses used in calculating averages; Textural zones refer to those shown in Figure 1b.

Figure 1

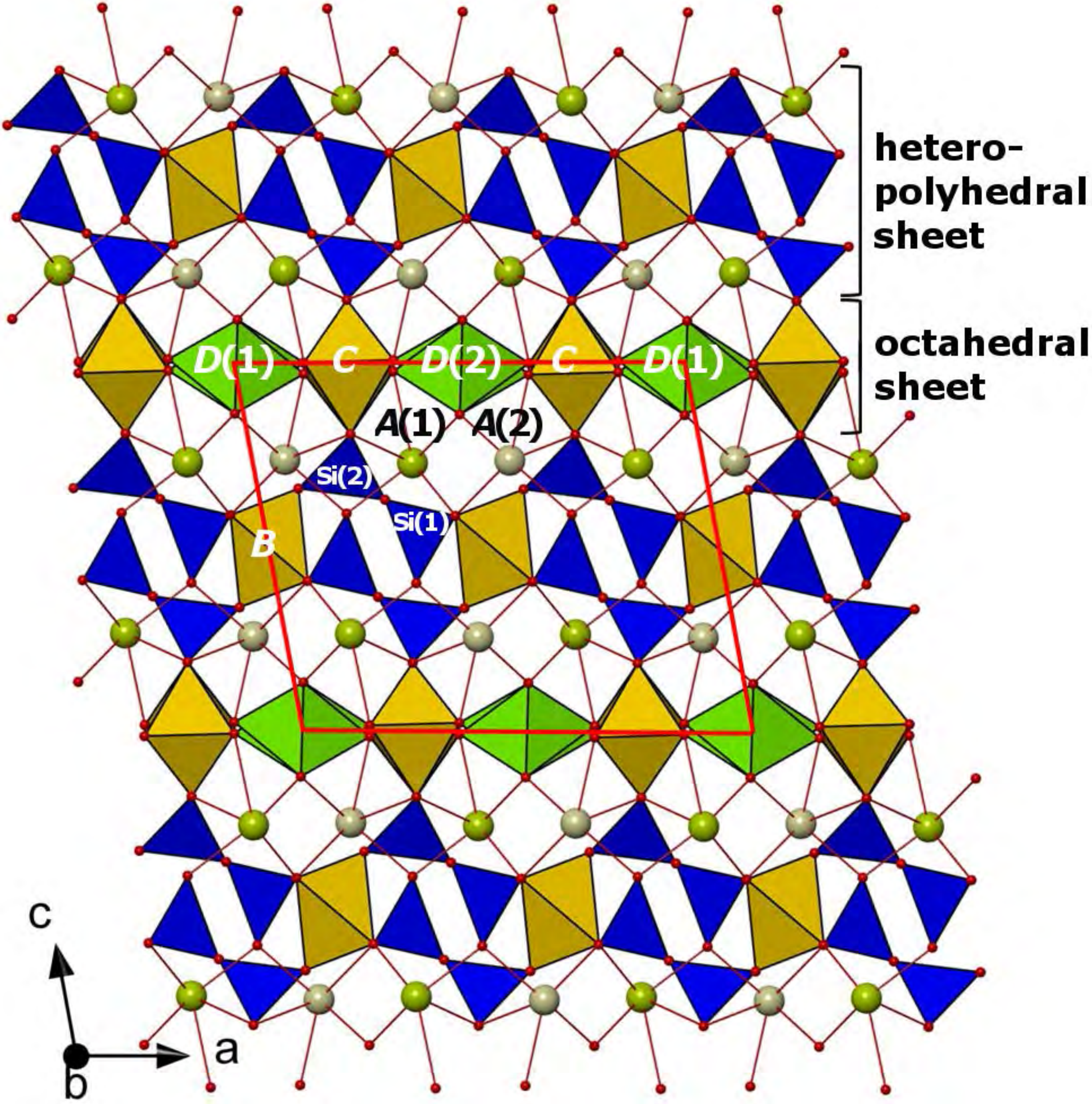
hetero-
polyhedral
sheet
octahedral
sheet
D(1)
C
D(2)
C
D(1)
A(1)
A(2)
Si(2)
Si(1)
B
c
a
b

Figure 2

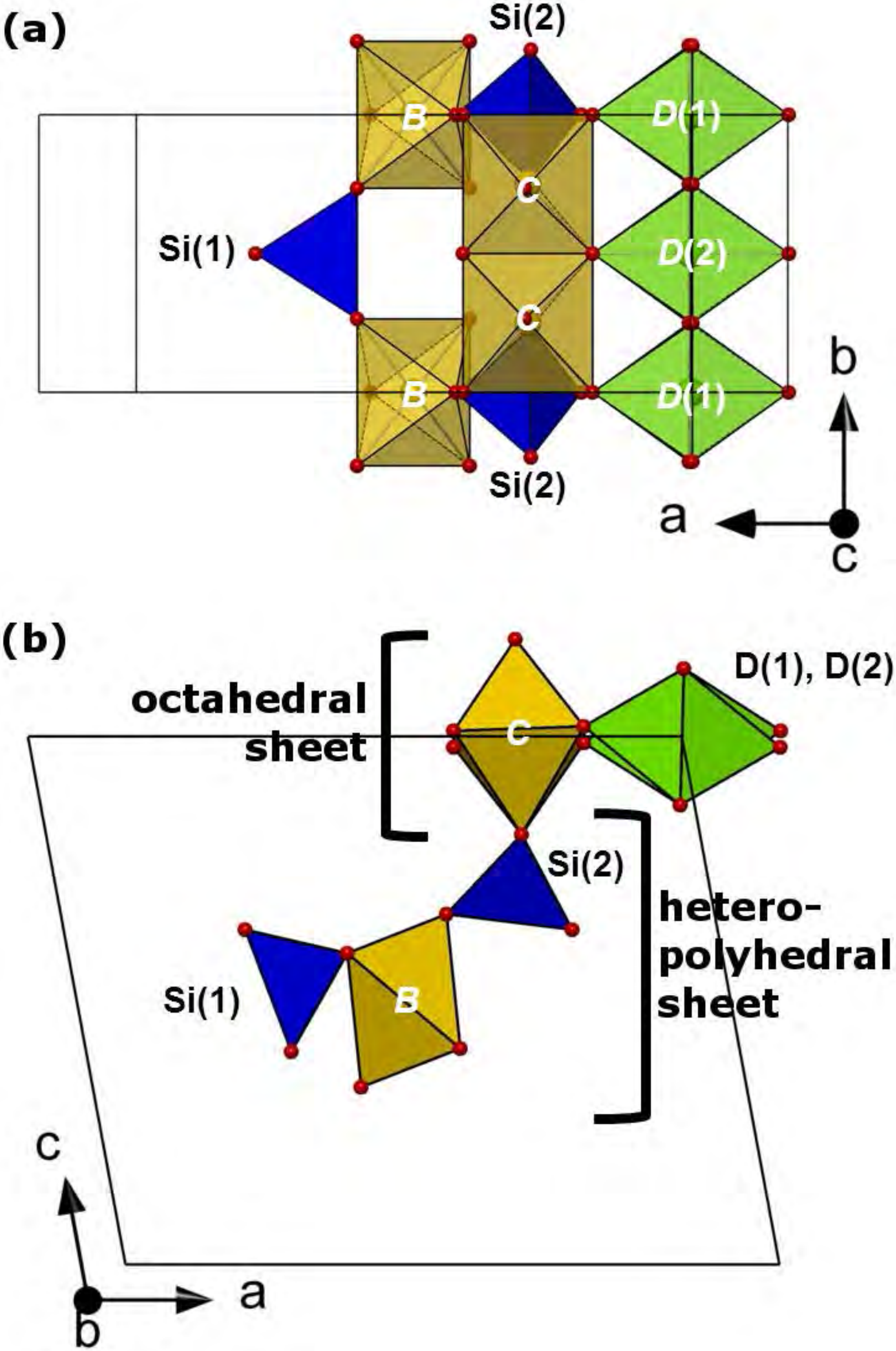
(a)
Si(2)
B
D(1)
C
Si(1)
D(2)
C
B
D(1)
Si(2)
b
a
c
(b)
octahedral sheet
C
D(1), D(2)
Si(2)
hetero-polyhedral sheet
Si(1)
B
c
a
b

Figure 3

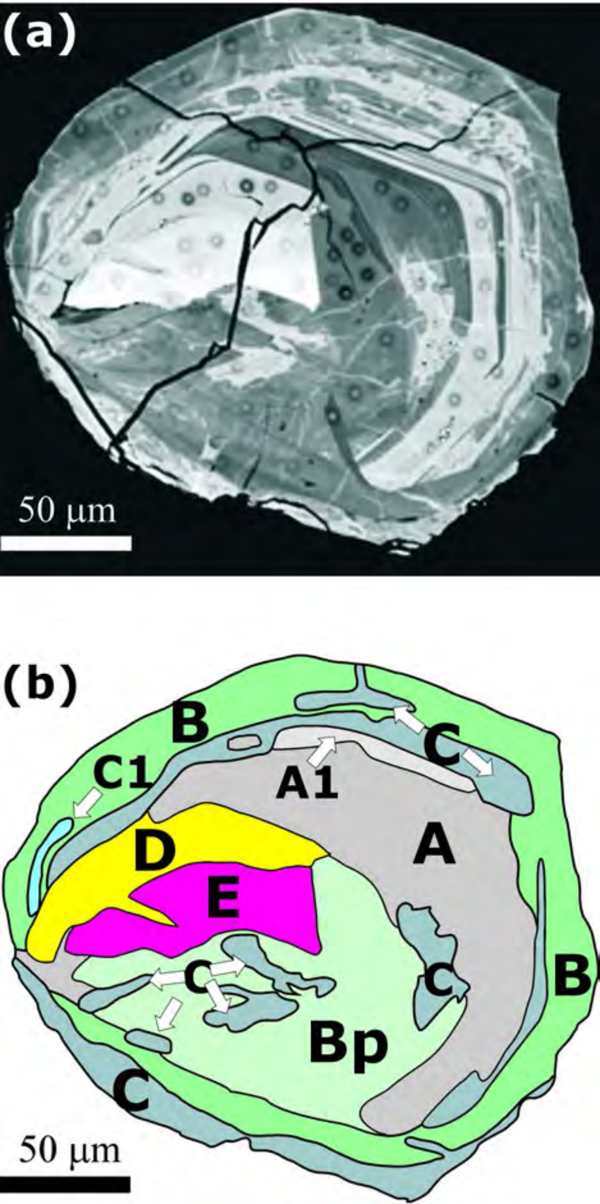

Figure 4

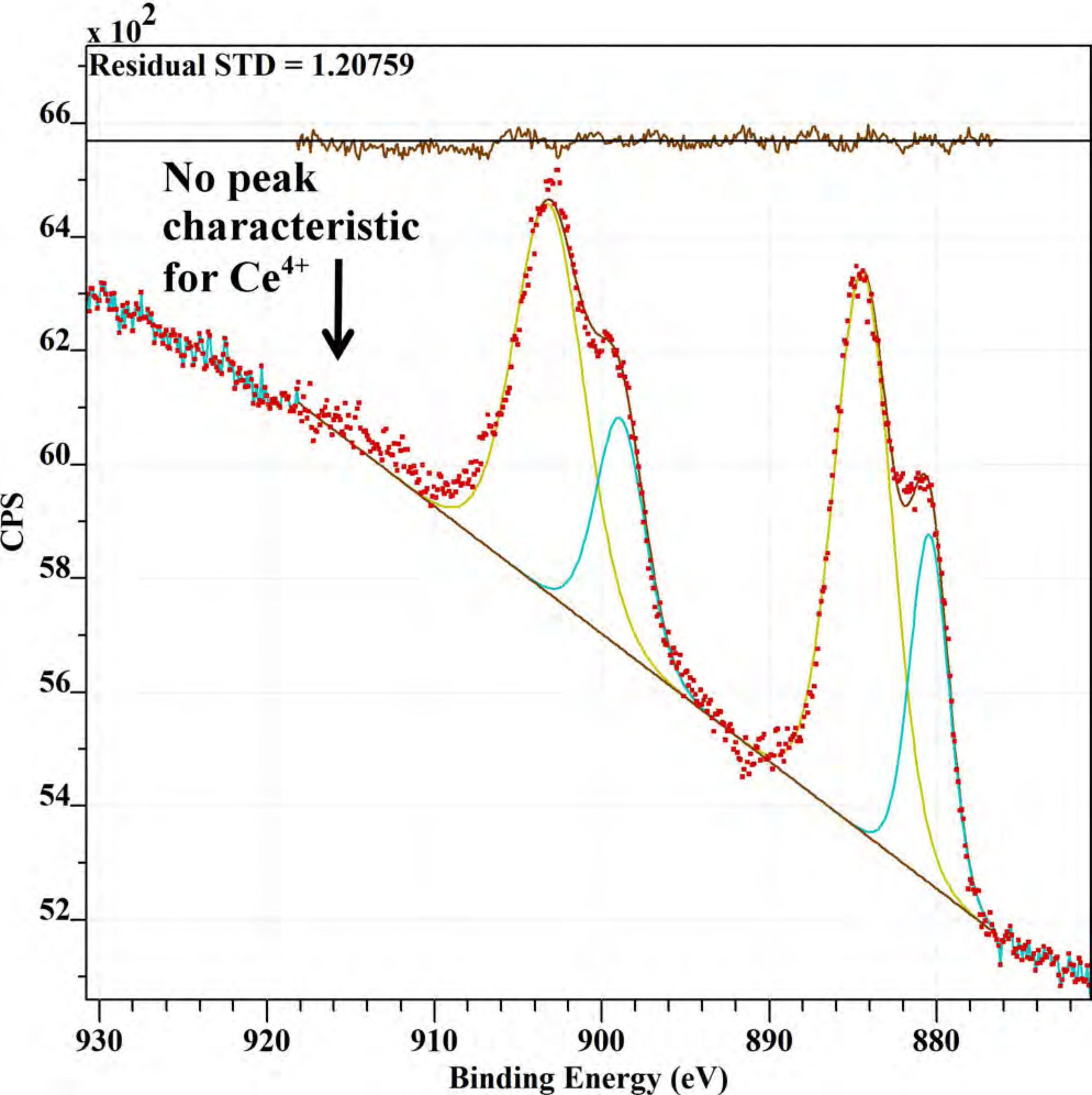
x 10^2
Residual STD = 1.20759
No peak characteristic for Ce4+
66
64
62
60
58
56
54
52
CPS
930
920
910
900
890
880
Binding Energy (eV)

Figure 5a

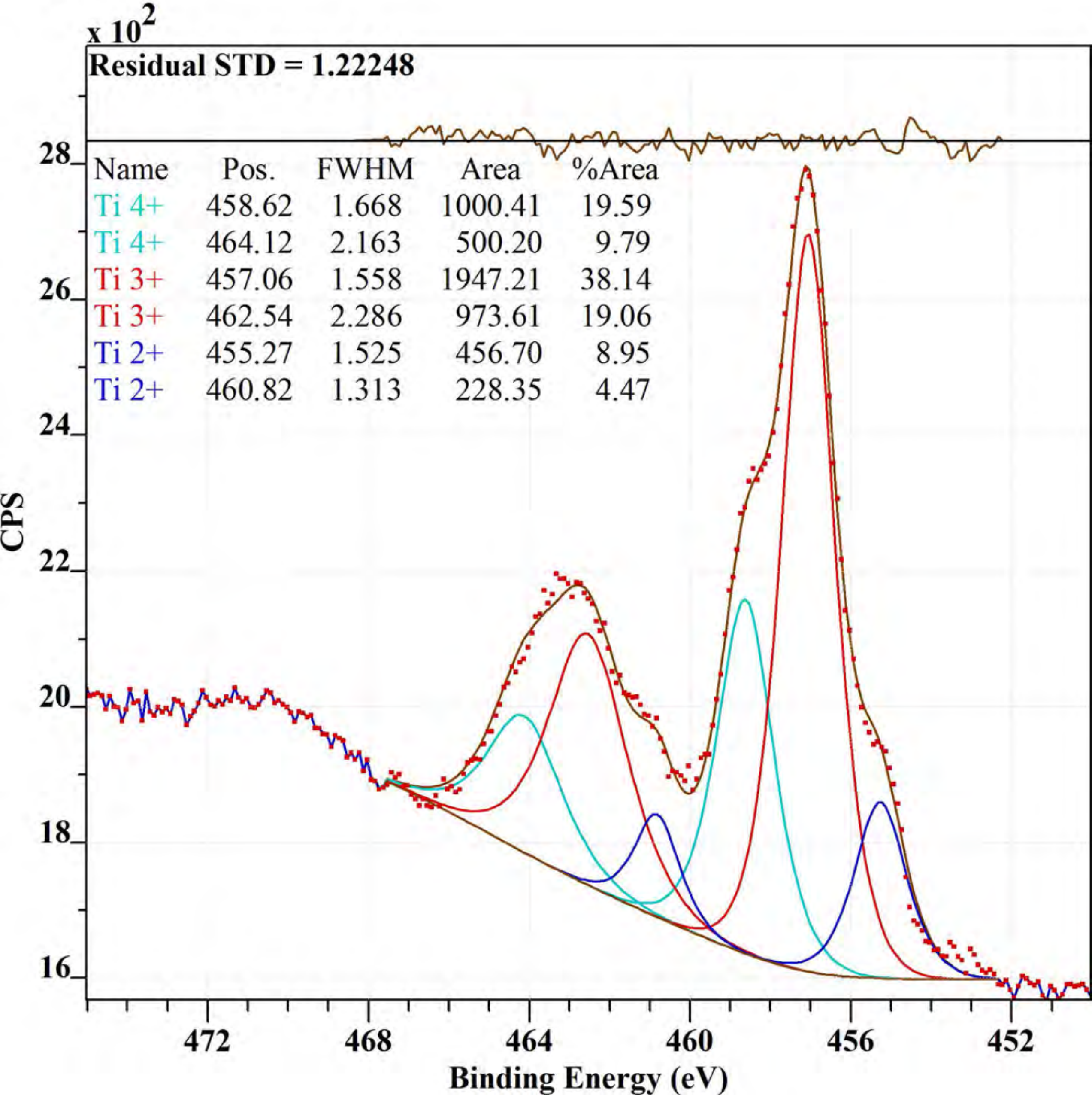

Name	Pos.	FWHM	Area	%Area
Ti 4+	458.62	1.668	1000.41	19.59
Ti 4+	464.12	2.163	500.20	9.79
Ti 3+	457.06	1.558	1947.21	38.14
Ti 3+	462.54	2.286	973.61	19.06
Ti 2+	455.27	1.525	456.70	8.95
Ti 2+	460.82	1.313	228.35	4.47

Figure 5b

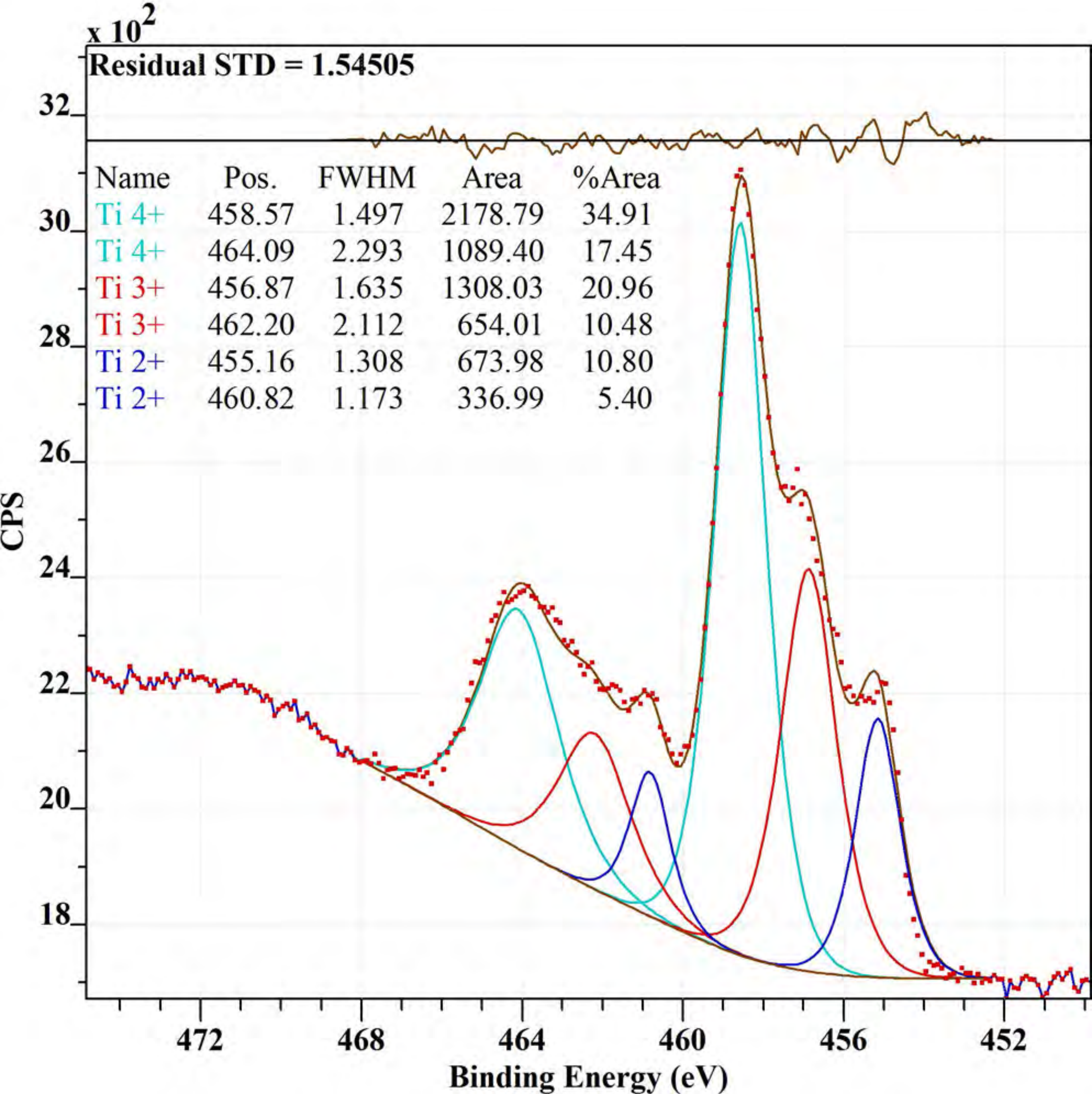

Name	Pos.	FWHM	Area	%Area
Ti 4+	458.57	1.497	2178.79	34.91
Ti 4+	464.09	2.293	1089.40	17.45
Ti 3+	456.87	1.635	1308.03	20.96
Ti 3+	462.20	2.112	654.01	10.48
Ti 2+	455.16	1.308	673.98	10.80
Ti 2+	460.82	1.173	336.99	5.40

Figure 6

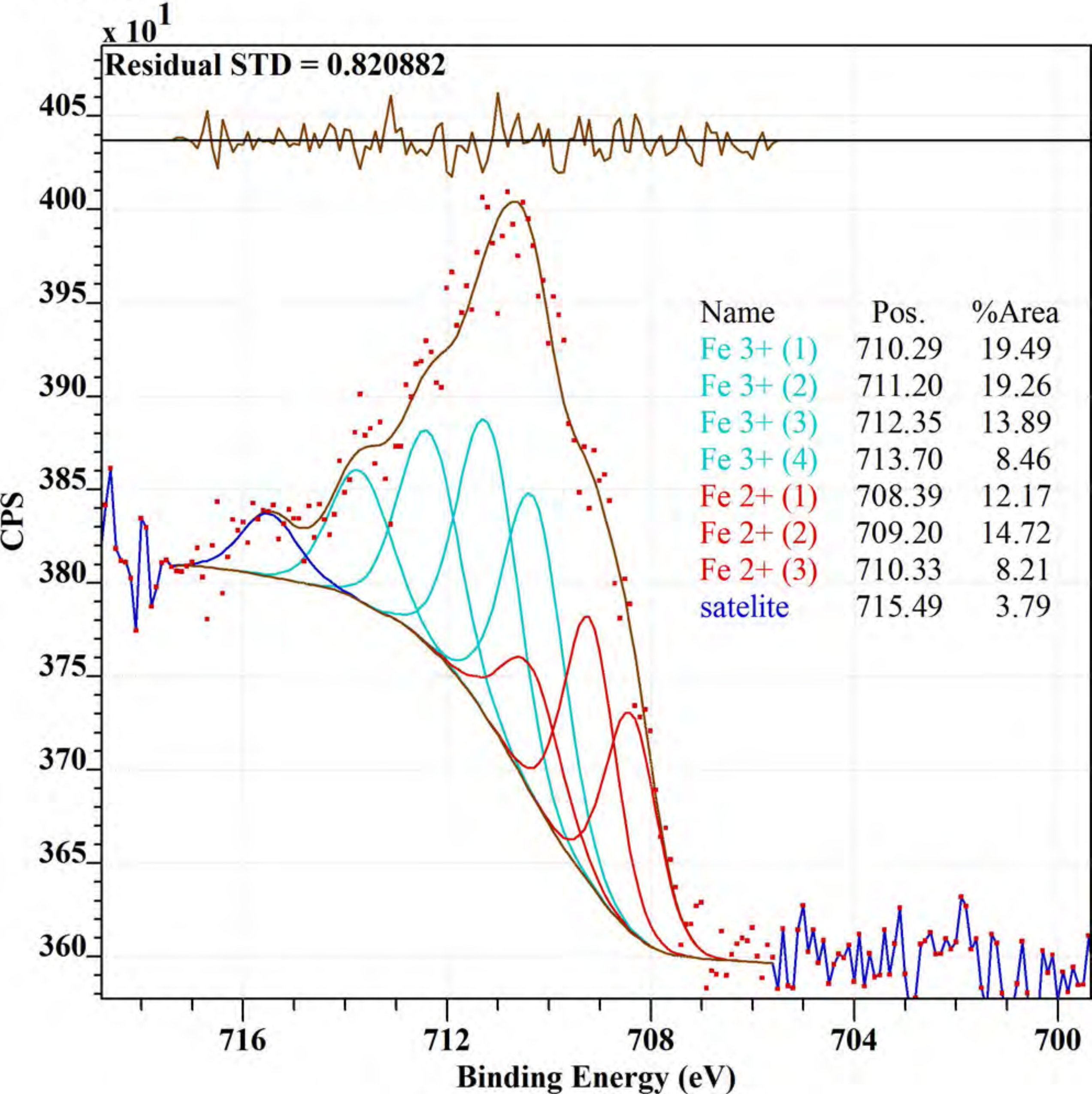

Name	Pos.	%Area
Fe 3+ (1)	710.29	19.49
Fe 3+ (2)	711.20	19.26
Fe 3+ (3)	712.35	13.89
Fe 3+ (4)	713.70	8.46
Fe 2+ (1)	708.39	12.17
Fe 2+ (2)	709.20	14.72
Fe 2+ (3)	710.33	8.21
satelite	715.49	3.79